Low-bias negative differential resistance in graphene nanoribbon superlattices

Gerson J. Ferreira,[1,2] Michael N. Leuenberger,[2] Daniel Loss,[3] and J. Carlos Egues[1,3]

[1]*Departamento de Física e Informática, Instituto de Física de São Carlos, Universidade de São Paulo, 13560-970 São Carlos, São Paulo, Brazil*

[2]*NanoScience Technology Center and Department of Physics, University of Central Florida, 12424 Research Parkway Suite 400, Orlando, Florida 32826, USA*

[3]*Department of Physics, University of Basel, Klingelbergstrasse 82, CH-4056 Basel, Switzerland*

(Received 24 May 2011; revised manuscript received 3 September 2011; published 30 September 2011)

We theoretically investigate negative differential resistance (NDR) for ballistic transport in semiconducting armchair graphene nanoribbon (aGNR) superlattices (5 to 20 barriers) at low bias voltages $V_{SD} < 500$ mV. We combine the graphene Dirac Hamiltonian with the Landauer-Büttiker formalism to calculate the current I_{SD} through the system. We find three distinct transport regimes in which NDR occurs: (i) a "classical" regime for wide layers, through which the transport across band gaps is strongly suppressed, leading to alternating regions of nearly unity and zero transmission probabilities as a function of V_{SD} due to crossing of band gaps from different layers; (ii) a quantum regime dominated by superlattice miniband conduction, with current suppression arising from the misalignment of miniband states with increasing V_{SD}; and (iii) a Wannier-Stark ladder regime with current peaks occurring at the crossings of Wannier-Stark rungs from distinct ladders. We observe NDR at voltage biases as low as 10 mV with a high current density, making the aGNR superlattices attractive for device applications.

DOI: 10.1103/PhysRevB.84.125453 PACS number(s): 72.80.Vp, 68.65.Cd, 73.21.Cd, 73.22.Pr

I. INTRODUCTION

Graphene[1–3] has attracted much attention due to the possibility of new devices that may surpass their semiconductor counterparts in both speed and reduced power consumption.[4] This is expected due to the unique properties of graphene, e.g., the high mobility of carriers, which can lead to high current densities, and the tunability of the band gap. Additionally, building devices on the surface could facilitate optical absorption and emission. Particularly, negative differential resistance (NDR) is essential for many applications.[5–8] In semiconductor resonant tunneling diodes[9–11] and superlattice structures,[12,13] NDR is based on Fabry-Pérot-type interferences arising from the impedance mismatch between the various layers. These semiconductor NDR systems can also show interesting phenomena, such as intrinsic bistability due to charge accumulation.[14] Pursuing the recent interest in graphene superlattices transport and thermal properties,[15–24] it is a natural question to ask whether a graphene superlattice could exhibit similar features.

The occurrence of Klein tunneling in graphene[2] should be an obstacle to the NDR effect, as it gives a monotonically increasing contribution to the current. Narrow graphene nanoribbons overcome this limitation as the lateral confinement quantizes the Dirac cone into few-eV-wide bands. Tight-binding calculations show that it is possible to find NDR in these narrow nanoribbons at high bias voltages, 1–2 V.[25,26] However, for integrated circuits a low bias mV regime is desirable to reduce power consumption.[27] Low bias NDR can also be achieved in other graphene and bilayer graphene systems.[28–30]

In this work we consider an N-barrier superlattice potential on a semiconducting armchair graphene nanoribbon (aGNR); Fig. 1. The electronic structure of the aGNR is a quantized Dirac cone, due to the quantization of the transversal momentum k_n, and can be metallic, $k_{n_0} = 0$, or semiconducting, $k_{n_0} \neq 0$, depending on the width W of the nanoribbon; k_{n_0} is the closest to zero transverse momenta. We choose $W = 346a_0$, such that the aGNR is semiconducting with a band gap

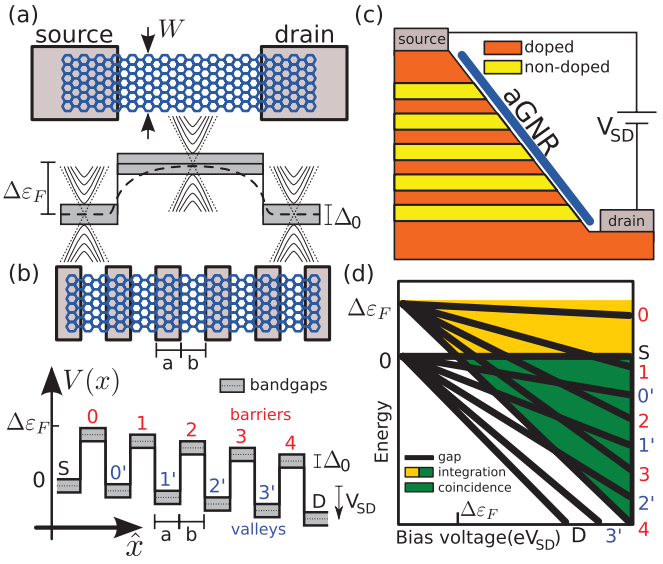

FIG. 1. (Color online) (a) Metal-aGNR junctions and the modulated chemical shift $\Delta\varepsilon_F$ of the Dirac point across the aGNR (Refs. 31–34). Δ_0 (shaded regions) denotes the barrier and valley band gaps. Here we consider square potentials, solid line. The dashed line shows the numerical results of Ref. 33. (b) Additional electrodes modulate the Dirac cone shift into a superlattice potential. The bias voltage V_{SD} is also shown. (c) Doped layers of a semiconductor superlattice can also modulate the local potential. (d) Schematic of the $\varepsilon - V_{SD}$ diagram of the source-drain transmission coefficient showing crossings of the band gaps Δ_0 (black lines). The shaded regions delimit the energy range between the source $\mu_S = \Delta\varepsilon_F$ and drain $\mu_D = \mu_S - eV_{SD}$ chemical potentials.

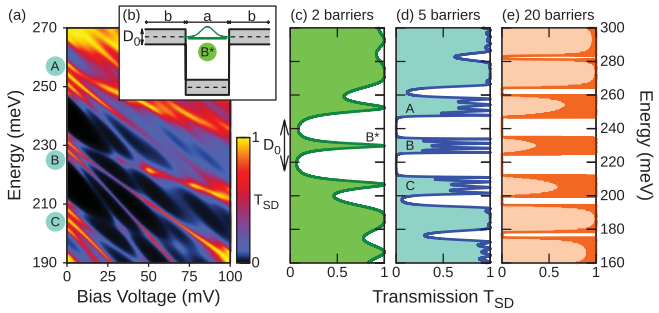

FIG. 2. (Color online) (a) Energy-voltage diagram of T_{SD} for $N = 5$ barriers showing the evolution of the $N-1$ hybridized modes [panels (b)–(d)] into Wannier-Stark ladders. Labels A, B, and C show the zero-bias hybridized modes in panels (a) and (d). Crossings of ladders' rungs from distinct minibands increases T_{SD} near $V_{SD} = 30$ and 50 mV. (b) Schematic of the modulated Dirac point (dashed line), band gaps $\Delta_0 \sim 28$ meV (gray area), and confined mode B'. In the transmission coefficient T_{SD} across two barriers ($a = b = 50$ nm) (c), the confined mode B' shows up as a resonant spike near 230 meV. For (d) $N = 5$, and (e) $N = 20$ barriers the confined modes hybridize into $N-1$ spikes, building up a miniband. Similar resonances lead to minibands at energies away from the band-gap region Δ_0.

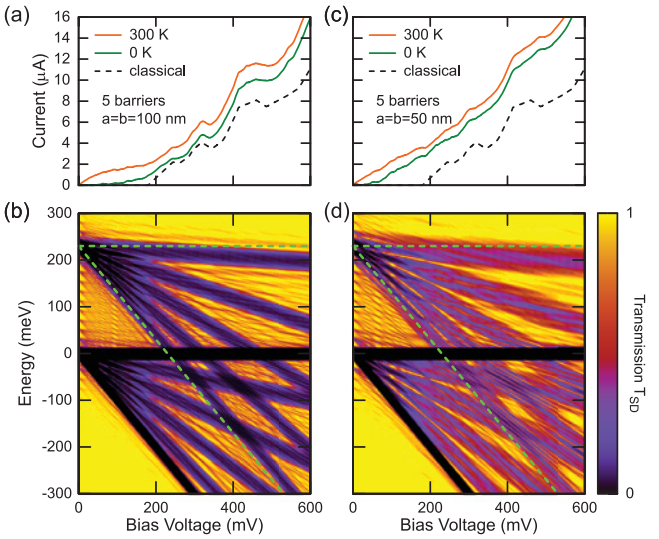

FIG. 3. (Color online) Current and energy-voltage diagram of the transmission coefficient for five-barrier superlattice with $a = b = 100$ nm [(a) and (b)] and $a = b = 50$ nm [(c) and (d)]. The current-voltage characteristics are shown for $T = 300$ K and 0 K. For wide barriers (a) and (b) the current follows closely the limiting "classical" case of T_{SD} either 0 across band gaps, or 1 otherwise (dashed line).

$\Delta_0 = 28$ meV; $a_0 = 0.142$ nm is the C-C distance. We use the transfer-matrix formalism to calculate the source-drain transmission coefficient T_{SD} across the superlattice potential along the aGNR, considering a finite bias voltage V_{SD}, revealing the electronic structure of the system; Fig. 2. The potential drop from source to drain follows a piecewise constant profile layer by layer; Fig. 1(b). The current is calculated within the usual Landauer-Büttiker formalism.

We find low bias NDR at zero and room temperatures within three distinct physical regimes. (i) For wide layers, the transmission across the band gaps Δ_0 is strongly suppressed, and nearly unity for energies away from the band gaps. With increasing voltage, both barrier and valley band gaps split and cross as shown schematically in Fig. 1(d), showing, at the coincidence region, a pattern of diamond-shaped structures with alternating regions of finite and suppressed transmission, thus leading to NDR. For narrow barriers resonant tunneling across layers become relevant. (ii) At zero bias, hybridization of resonant modes leads to minibands with finite, nearly unity, transmission; Figs. 2(b)–2(e). At very low voltages $eV_{SD} \sim 10$ meV (of the order of the miniband energy width) the resonant states misalign, thus breaking the minibands into off-resonance Wannier-Stark ladders with suppressed transmission. This gives rise to a single current spike near $eV_{SD} \sim 10$ meV. (iii) With increasing eV_{SD}, rungs of ladders from distinct minibands cross and hybridize, showing a new set of resonant spikes in T_{SD}, Fig. 2(a), thus leading to current spikes and NDR.

II. PROPOSED SYSTEM AND MODEL

The modulation of the Dirac cone into a superlattice potential can be achieved by different setups. It was shown that local charge-transfer effects between graphene and some metals (e.g., Al, Cu, Ag, Au, Pt) rigidly shifts the Dirac cone;[31–34] Fig. 1(a). A series of metallic stripes over graphene can create the proposed superlattice potential; Fig. 1(b). Equivalently, the same structure can be obtained by selectively doping graphene regions in an alternate fashion. Additionally, the aGNR could be arranged along the doped/nondoped layers of a cleaved semiconductor heterostructure;[35] Fig. 1(c). Narrow systems ($\lesssim$400 nm) are desirable to keep transport ballistic at room temperatures.

We consider low-energy excitations of graphene within the envelope function approximation,[3,36] i.e., the graphene Dirac Hamiltonian. The finite size of the nanoribbon requires vanishing wave functions at the edges, where for aGNR both A and B sublattices of the honeycomb lattice are present. This leads to vanishing boundary conditions for the envelope functions at these edges.[3] The validity of these boundary conditions is discussed in Ref. 37. Within this description, the electronic structure of an aGNR is a quantized Dirac cone, $\varepsilon = s\hbar v_f \sqrt{k_x^2 + k_n^2}$. Here $s = \pm 1$ for the conduction and valence bands, $v_f \approx 10^{15}$ nm/s is the Fermi velocity, k_x is the momentum in the longitudinal direction $\hat{x}$, $k_n = n\pi/W - 4\pi/3a_0$ is the quantized transverse momentum with integer n, and $W = 346a_0 \sim 50$ nm. The fundamental gap is given by $\Delta_0 = 2\hbar v_f |k_{n_0}| = 28$ meV, with $k_{n_0} \sim -0.021$ nm^{-1}.

To calculate the transmission $T_{SD} \equiv T_{SD}(\varepsilon, k_n, V_{SD})$ we use the transfer-matrix formalism,[38] which relates the coefficients of the incoming and outgoing plane waves at the source and drain leads across the superlattice layers (see the Appendix for details). We consider a piecewise constant superlattice potential along the x direction, Figs. 1(b), through which the electronic structure of each layer is shifted by the local potential. In Figs. 2–4 we show T_{SD} only for k_{n_0}, as it contains the major contribution for the current in all investigated cases.

The current density of Dirac electrons in graphene is given by $\vec{j}(\mathbf{r}) = 4ev_f \psi^\dagger(\mathbf{r})\vec{\sigma}\psi(\mathbf{r})$, where the factor of 4 accounts

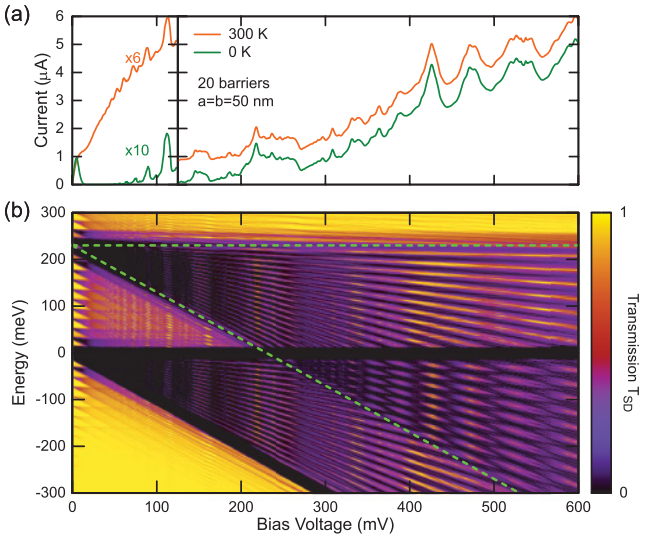

FIG. 4. (Color online) (a) Current-voltage characteristics and (b) T_{SD} diagram of a 20-barrier aGNR superlattice with $a = b = 50$ nm. In (a) the currents for 0 and 300 K in the range $0 \leqslant V_{SD} \leqslant 125$ mV are multiplied by 6 and 10, respectively, for clarity. As the voltage increases the miniband near 230 meV, Fig. 2(e), breaks up as the resonant levels misalign, leading to the pronounced spike near 10 mV for 0 K. Near 50 mV the resonant levels return as resonant crossings of Wannier-Stark ladder rungs [see also Fig. 2(a)]. At the crossings T_{SD} increases, showing current spikes at both 0 and 300 K for $V_{SD} < 230$ mV. For $V_{SD} > 230$ mV the current spikes arise from crossings of rungs at the coincidence region.

for the valley and spin degeneracies, $\psi(\mathbf{r})$ is the envelope function spinor for the K or K' valley, and $\vec{\sigma} = (\sigma_x, \sigma_y)$ are the Pauli matrices. Within the Landauer-Büttiker formalism,[38,39] the current reads

$$I_{SD} = \frac{e}{h} \sum_n \int_{-\infty}^{\infty} T_{SD}(\varepsilon, k_n, V_{SD}) \, [f_S(\varepsilon) - f_D(\varepsilon)] \, d\varepsilon, \qquad (1)$$

where $f_S(\varepsilon) = \{1 + \exp[(\varepsilon - \mu_S)/k_B T]\}^{-1}$ and $f_D(\varepsilon) = f_S(\varepsilon + V_{SD})$ are the Fermi-Dirac distributions at the source and drain, and μ_S is the source chemical potential. We truncate the sum over n to a few k_n near k_{n_0}.

III. RESULTS

In Fig. 2(b) we consider a narrow graphene well with $a = 50$ nm and $b \to \infty$. The solution of the graphene Dirac equation within the band-gap Δ_0 region shows a confined state.[40] This state corresponds to the resonant spike within the Δ_0 region in Fig. 2(b) for two barriers. For N barriers the confined states hybridizes into $N - 1$ states, leading to minibands for large N; Figs. 2(c) and 2(d). The minibands away from the Δ_0 region occur due to reflections at each interface. For finite bias the minibands break into single resonant levels, Wannier-Stark ladders, as the confined modes from each layer misalign; Fig. 2(e). At the crossings of Wannier-Stark ladders from distinct minibands the transmission increases due to resonant tunneling.

A. NDR regimes

To contrast distinct NDR regimes in our system, we discuss the current-voltage characteristics I-V_{SD} and the energy-voltage T_{SD} diagram for the following three cases. We compare five-barrier superlattices with (i) wide layers [Figs. 3(a) and 3(b)] and (ii) narrow layers [Figs. 3(c) and 3(d)]. We then discuss (iii) a 20-barrier superlattice with narrow layers; Fig. 4. The dashed lines in the T_{SD} diagrams delimit the zero-temperature window of integration for I_{SD}, defined between the source $\mu_S = 230$ meV and drain $\mu_D = \mu_S - V_{SD}$ chemical potentials.

1. *"Classical" regime*

For wide layers, $a = b = 100$ nm, tunneling across band gaps is strongly suppressed and the T_{SD} diagram, Fig. 3(b), follows closely the diamond pattern in Fig. 1(d). For $eV_{SD} \lesssim \Delta\varepsilon_F = 230$ meV the current increases monotonically as the barriers band gaps misalign. At the coincidence region, $eV_{SD} \gtrsim \Delta\varepsilon_F = 230$ meV, crossings of barrier and valley band gaps lead to the diamond pattern of finite and suppressed T_{SD}. This alternation leads to the NDR near $V_{SD} = 350$ and 450 mV, in Fig. 3(a). The intensity of the NDR in this regime increases with the layers width, as the tunneling across band gaps becomes more suppressed. The dashed curve in Fig. 3(a) is calculated with the limiting case where tunneling is completely suppressed across band gaps, i.e., $T_{SD}^{\text{classical}} = 0$ across a band gap, and 1 otherwise. Note the similarity of the dashed classical line with the exact I_{SD} calculations in Fig. 3(a).

For narrow layers, $a = b = 50$ nm in Figs. 3(c) and 3(d), the NDR due to classical regime is absent as it requires strong tunneling suppression. Interestingly, however, the T_{SD} diagram of a few narrow layers clearly shows the evolution of the zero-bias minibands into Wannier-Stark ladders with increasing V_{SD}; Fig. 2(e). The Wannier-Stark ladders remain as individual transmission spikes while there is an overlap of barriers (or valley) band gaps. For $eV_{SD} > (N - 1/2)\Delta_0$ this condition is violated, and the tunneling across individual band gaps dominate. At the crossings of barrier and valley band gaps, resonant effects are still visible in the T_{SD} diagram as stripes, corresponding to confined states between the overlapping band gaps; see Fig. 3(d) near $\varepsilon = -50$ meV and $V_{SD} = 400$ mV.

2. *Miniband regime*

Considering a larger number of barriers, $N = 20$ in Fig. 4, the aligned resonant modes hybridize into superlattice minibands; Fig. 2. If μ_S is located within the miniband, at low biases the current is dominated by the transmission across these resonant modes. As the bias increases, the modes misalign breaking up the miniband into Wannier-Stark ladders. For five barriers, Fig. 2(a), the rungs of the ladders shows nonresonant transmission peaks, and enhanced resonant transmission at crossings of the rungs (see *Wannier-Stark ladder regime* below). For 20 barriers, transmission through nonresonant rungs is strongly suppressed due to the larger number of band gaps. At very low voltages, Fig. 4, the current initially increases with V_{SD} as the transport occurs through the miniband. Near $eV_{SD} \sim 10$ meV (of the order of the miniband width) the

miniband breaks up into the nonresonant rungs suppressing the current, thus resulting in a pronounced current peak.

3. Wannier-Stark ladder regime

With increasing bias, rungs from Wannier-Stark ladders of distinct minibands cross, Fig. 2(a), creating new resonances through the superlattice layers. For 20 barriers, where transmission from nonresonant rungs is strongly suppressed, the crossings show sharp $T_{\rm SD}$ stripes, e.g., at $V_{\rm SD} = 75$, 110, 150, and 210 mV; Fig. 4(b). Each of these stripes, and others with lower contrast at smaller voltages, leads to current spikes in Fig. 4(a). The spikes broaden with increasing bias as the band gaps misalign. For $eV_{\rm SD} > \Delta\varepsilon_{\rm F} = 230$ meV, the crossings of broadened Wannier-Stark ladders from minibands near the barrier and valley band gaps show diamond-shaped structures in the $T_{\rm SD}$ diagram, thus leading to a series of NDR spikes similar to the classical regime.

IV. CONCLUSIONS

We have found that three distinct regimes can lead to NDR in semiconducting aGNR superlattices. (i) In the classical regime the NDR occurs as the band gaps of different layers cross with increasing $V_{\rm SD}$. (ii) For narrow layers and very low biases, $eV_{\rm SD} \sim 10$ meV, the transport is dominated by the resonant tunneling through the miniband, and the NDR occurs as the miniband breaks into Wannier-Stark ladders with increasing bias. (iii) For higher bias rungs of distinct ladders cross originating new resonances and current peaks. Interestingly, due to the high mobility of the carriers, we obtain low bias NDR peaks with high current densities.

A. Final remarks

The predicted NDR effects reported here are strictly valid for ballistic electronic transport through ideal aGNR superlattices. For relatively clean systems, however, we expect detrimental effects such as those induced by disorder, impurities and structural defects[23,24,41,42] to broaden the resonances in the I-V curves, thus possibly reducing the peak-to-valley current ratios. Interestingly, a recent calculation for the electronic transport through a single-barrier defined on a zigzag-terminated graphene nanoribbon shows evidence for a transport gap despite the gapless spectrum of the edge states of the system.[43] Therefore we expect that a superlattice defined on a zigzag graphene nanoribbon should exhibit transport features similar to those of the armchair case investigated here. The effects of edge irregularities, strong disorder, and interactions (even at the Hartree level) lie beyond the scope of the present work and deserve further study.

ACKNOWLEDGMENTS

We thank Björn Trauzettel, Saiful Khondaker, Volodymyr Turkowski, and Stephano Chesi for useful discussions. The authors acknowledge support from FAPESP, CNPq, Swiss NSF, and NCCR Nanoscience. M.N.L. acknowledges support from NSF (Grant No. ECCS-0725514), DARPA/MTO (Grant No. HR0011-08-1-0059), NSF (Grant No. ECCS-0901784), and AFOSR (Grant No. FA9550-09-1-0450).

APPENDIX: TRANSFER MATRIX

In this Appendix we detail the calculation of the transmission coefficient $T_{\rm SD}$ through the nanoribbon superlattice via the transfer-matrix approach. We describe the potential across the system as piecewise constant; Fig. 1(b). In each layer the potential is a constant $V_j = V_j^{\rm SL} - eV_{\rm SD}x_j/L$. The superlattice potential $V_j^{\rm SL}$ is 0 for valleys, and $V_{\rm b} = 230$ mV for barriers (typical value obtained from Refs. 31–34). The second term is the potential energy drop across the jth layers due to the electric field, where x_j is the coordinate of the center of the layer j, and L is the distance between the source and drain.

The solution of the Dirac equation in each layer j ($j = $ S and D for the source and drain, and an integer for the intermediate layers) is given by the plane-wave spinors[2,3] $\psi_{j,n}(x,y) = e^{ik_n y}\varphi_j(x)$. For convenience we write the x component in a matrix form $\varphi_j(x) = M_j(x)\phi_j$, where the components of the spinor $\phi_j^{\rm T} = (\alpha_j \;\; \beta_j)^T$ denote the coefficients of the outgoing and incoming plane waves. The matrix $M_j(x)$ is

$$M_j(x) = \begin{pmatrix} e^{ik_x^{(j)}x} & e^{-ik_x^{(j)}x} \\ s_j e^{ik_x^{(j)}x+i\theta_{j,n}} & -s_j e^{-ik_x^{(j)}x-i\theta_{j,n}} \end{pmatrix}. \tag{A1}$$

The eigenenergies in each layer are $\varepsilon_{j,n} = V_j + s_j\hbar v_{\rm f}\sqrt{(k_x^{(j)})^2 + k_n^2}$, with $s_j = +1$ for the conduction band and $s_j = -1$ for the valence band, $k_x^{(j)}$ is the longitudinal momentum in layer j, k_n is the quantized transversal momentum (conserved through the system), and $\theta_{j,n} = \tan^{-1}(k_n/k_x^{(j)})$.

The continuity of the spinors at the interfaces yields $\varphi_j(x_{j,j+1}) = \varphi_{j+1}(x_{j,j+1})$, where $x_{j,j+1}$ is the position of the interface between the layers j and $j+1$. Applying this matching throughout the system, we obtain a 2×2 matrix equation connecting the coefficients from source and drain $\phi_{\rm S} = T_{\rm M}\phi_{\rm D}$, where $T_{\rm M}$ is the transfer matrix given by

$$T_{\rm M} = \prod_j M_j^{-1}(x_{j,j+1})M_{j+1}(x_{j,j+1}). \tag{A2}$$

The definition of the reflected and transmitted waves depends on the sign of the electron energy at source $s_{\rm S}$ and drain $s_{\rm D}$, such that the source and drain coefficients are given by

$$\phi_{\rm S}^{\rm T} = \begin{cases} (1 \;\; r), & \text{if } s_{\rm S} = +1, \\ (r \;\; 1), & \text{if } s_{\rm S} = -1, \end{cases} \tag{A3}$$

$$\phi_{\rm D}^{\rm T} = \begin{cases} (t \;\; 0), & \text{if } s_{\rm D} = +1, \\ (0 \;\; t), & \text{if } s_{\rm D} = -1. \end{cases} \tag{A4}$$

From the graphene Dirac Hamiltonian, the current density reads $J_x^{(j)} = 4ev_{\rm f}\varphi_j^\dagger(x)\sigma_x\varphi_j(x)$. At the stationary regime the current flow at source and drain is the same, requiring the match $J_x^{\rm S} = J_x^{\rm D}$, from which we identify the transmission coefficient $T_{\rm SD}$,

$$T_{\rm SD}(\varepsilon,k_n,V_{\rm SD}) = |t|^2\frac{\cos\theta_{\rm D}}{\cos\theta_{\rm S}}. \tag{A5}$$

This transmission coefficient as a function of the energy reveals the electronic structure of the system, in which the confined modes in between the layers show up as resonant spikes and minibands; Fig. 2.

[1] K. S. Novoselov, A. K. Geim, S. V. Morozov, D. Jiang, M. I. Katsnelson, I. V. Grigorieva, S. V. Dubonos, and A. A. Firsov, Nature (London) **438**, 197 (2005).
[2] M. I. Katsnelson, K. S. Novoselov, and A. K. Gaim, Nat. Phys. **2**, 620 (2006).
[3] A. H. C. Neto, F. Guinea, N. M. R. Peres, K. S. Novoselov, and A. K. Gaim, Rev. Mod. Phys. **81**, 109 (2009).
[4] P. Avouris, Nano Lett. **10**, 4285 (2010).
[5] P. Y. Yu and M. Cardona, *Fundamentals of Semiconductors* (Springer, Berlin, 2005).
[6] A. Mortazawi, V. P. Kesan, D. P. Neikirk, and T. Itoh, in *Proceedings of the 19th European Microwave Conference* (IEEE, London, 1989), p. 715.
[7] T. C. L. G. Sollner, E. R. Brown, W. D. Goodhue, and C. A. Correa, J. Appl. Phys. **64**, 4248 (1988).
[8] S. M. Sze and K. K. Ng, *Physics of Semiconductor Devices* (Wiley-Interscience, New York, 2007).
[9] R. Tsu, Appl. Phys. Lett. **22**, 562 (1973).
[10] T. C. L. G. Sollner, Appl. Phys. Lett. **43**, 588 (1983).
[11] L. V. Iogansen, Zh. Eksp. Teor. Fiz. **45**, 207 (1963) [Sov. Phys.-JEPT **18**, 149 (1969)]; Zh. Eksp. Teor. Fiz. **47**, 270 (1964) [Sov. Phys.-JEPT **20**, 180 (1965)].
[12] L. Esaki and R. Tsu, IBM J. Res. Dev. **14**, 61 (1970).
[13] R. Tsu, *Superlattice to Nanoelectronics* (Elsevier, Amsterdam, 2005).
[14] V. J. Goldman, D. C. Tsui, and J. E. Cunningham, Phys. Rev. Lett. **58**, 1256 (1987).
[15] C. Bai and X. Zhang, Phys. Rev. B **76**, 075430 (2007).
[16] L. Brey and H. A. Fertig, Phys. Rev. Lett. **103**, 046809 (2009).
[17] C. H. Park, Y. W. Son, L. Yang, M. L. Cohen, and S. G. Louie, Phys. Rev. Lett. **103**, 046808 (2009).
[18] M. Barbier, P. Vasilopoulos, and F. M. Peeters, Phys. Rev. B **81**, 075438 (2010).
[19] V. M. Stojanović, N. Vukmirović, and C. Bruder, Phys. Rev. B **82**, 165410 (2010).
[20] P. Burset, A. L. Yeyati, L. Brey, and H. A. Fertig, Phys. Rev. B **83**, 195434 (2011).
[21] X. Guo, D. Liu, and Y. Li, Appl. Phys. Lett. **98**, 242101 (2011).
[22] J. Jiang, J. Wang, and B. Wang, Appl. Phys. Lett. **99**, 043109 (2011).
[23] N. Abedpour, A. Esmailpour, R. Asgari, and M. R. Tabar, Phys. Rev. B **79**, 165412 (2009).
[24] H. Cheraghchi, A. H. Irani, S. M. Fazeli, and R. Asgari, Phys. Rev. B **83**, 235430 (2011).
[25] Z. F. Wang, Q. Li, Q. W. Shi, X. Wang, J. Yang, J. G. Hou, and J. Chen, Appl. Phys. Lett. **92**, 133114 (2008).
[26] V. N. Do and P. Dollfus, J. Appl. Phys. **107**, 063705 (2010).
[27] A recent work (Ref. 44) has claimed that low-bias NDR can be achieved with a single barrier in a infinite graphene sheet. This, however, has been disputed in Refs. 45 and 46.
[28] H. Ren, Q.-X. li, Y. Luo, and J. Yang, Appl. Phys. Lett. **94**, 173110 (2009).
[29] K. Habib, F. Zahid, and R. Lake, Appl. Phys. Lett. **98**, 192112 (2011).
[30] H. Fang, R. Wang, S. Chen, M. Yan, X. Song, and B. Wang, Appl. Phys. Lett. **98**, 082108 (2011).
[31] G. Giovannetti, P. A. Khomyakov, G. Brocks, V. M. Karpan, J. van den Brink, and P. J. Kelly, Phys. Rev. Lett. **101**, 026803 (2008).
[32] M. Vanin, J. J. Mortensen, A. K. Kelkkanen, J. M. Garcia-Lastra, K. S. Thygesen, and K. W. Jacobsen, Phys. Rev. B **81**, 081408(R) (2010).
[33] S. Barraza-Lopez, M. Vanević, M. Kindermann, and M. Y. Chou, Phys. Rev. Lett. **104**, 076807 (2010).
[34] A. Varykhalov, M. R. Scholz, T. K. Kim, and O. Rader, Phys. Rev. B **82**, 121101 (2010).
[35] R. Krahne, A. Yacoby, H. Shtrikman, I. Bar-Joseph, T. Dadosh, and J. Sperling, Appl. Phys. Lett. **81**, 730 (2002).
[36] P. R. Wallace, Phys. Rev. **71**, 622 (1947).
[37] L. Brey and H. A. Fertig, Phys. Rev. B **73**, 235411 (2006).
[38] S. Datta, *Electronic Transport in Mesoscopic Systems* (Cambridge University Press, Cambridge, England, 1997).
[39] Y. M. Blanter and M. Buttiker, Phys. Rep. **336**, 1 (2000).
[40] B. Trauzettel, D. V. Bulaev, D. Loss, and G. Burkard, Nat. Phys. **3**, 192 (2007).
[41] M. Han, J. Brant, and P. Kim, Phys. Rev. Lett. **104**, 056801 (2010).
[42] K. Saloriutta, Y. Hancock, A. Kärkkäinen, L. Kärkkäinen, M. J. Puska, and A. P. Jauho, Phys. Rev. B **83**, 205125 (2011).
[43] J. Nakabayashi, D. Yamamoto, and S. Kurihara, Phys. Rev. Lett. **102**, 066803 (2009).
[44] D. Dragoman and M. Dragoman, Appl. Phys. Lett. **90**, 143111 (2007).
[45] V. N. Do, Appl. Phys. Lett. **92**, 216101 (2008).
[46] V. N. Do, V. H. Nguyen, P. Dollfus, and A. Bournel, J. Appl. Phys. **104**, 063708 (2008).